Author Manuscript
Author Manuscript
Author Manuscript
Author Manuscript

HHS Public Access
Author manuscript
Nat Nanotechnol. Author manuscript; available in PMC 2020 December 06.

Published in final edited form as:
Nat Nanotechnol. 2020 December ; 15(12): 1053–1064. doi:10.1038/s41565-020-00782-3.

Proton-driven transformable nanovaccine for cancer immunotherapy

Ningqiang Gong[1,2,3,4], **Yuxuan Zhang**[2,4], **Xucong Teng**[1], **Yongchao Wang**[2], **Shuaidong Huo**[2,5], **Guangchao Qing**[2], **Qiankun Ni**[1,2,4], **Xianlei Li**[2,4], **Jinjin Wang**[2,4], **Xiaoxia Ye**[2], **Tingbin Zhang**[2], **Shizhu Chen**[2,6], **Yongji Wang**[1], **Jie Yu**[7], **Paul C. Wang**[2,8,9], **Yaling Gan**[2], **Jinchao Zhang**[6], **Michael J. Mitchell**[3], **Jinghong Li**[1], **Xing-Jie Liang**[2,4,6]

[1]Department of Chemistry, Key Laboratory of Bioorganic Phosphorus Chemistry and Chemical Biology, Tsinghua University, Beijing, China.

[2]Laboratory of Controllable Nanopharmaceuticals, Chinese Academy of Sciences (CAS) Center for Excellence in Nanoscience and CAS Key Laboratory for Biomedical Effects of Nanomaterials and Nanosafety, National Center for Nanoscience and Technology, Beijing, China.

[3]Department of Bioengineering, University of Pennsylvania, Philadelphia, PA, USA.

[4]University of Chinese Academy of Sciences, Beijing, China.

[5]Fujian Provincial Key Laboratory of Innovative Drug Target Research, School of Pharmaceutical Science, Xiamen University, Xiamen, China.

[6]Key Laboratory of Medicinal Chemistry and Molecular Diagnosis of the Ministry of Education, College of Chemistry and Environmental Science, Hebei University, Baoding, China.

[7]Department of Interventional Ultrasound, Chinese PLA General Hospital, Beijing, China.

[8]Laboratory of Molecular Imaging, Department of Radiology, Howard University, Washington DC, USA.

[9]Department of Electrical Engineering, Fu Jen Catholic University, Taipei, Taiwan.

Reprints and permissions information is available at www.nature.com/reprints.

jhli@mail.tsinghua.edu.cn; liangxj@nanoctr.cn.

Author contributions
N.G., J.L. and X.-J.L. conceived and designed the experiments. N.G., Y.Z., X.T., Yongchao Wang, S.H., G.Q., Q.N., X.L., J.W., X.Y., T.Z., S.C. and Yongji Wang performed the experiments. N.G., X.Y., T.Z., J.L. and X.-J.L. analysed the results. J.Y., Y.G., J.Z., P.C.W and M.J.M. developed the discussion. N.G., J.L. and X.-J.L. wrote the manuscript. J.L. and X.-J.L. supervised the entire project. All authors discussed the results and commented on the manuscript.

Data availability
All relevant data during the study are available from the corresponding authors upon request. Source data are provided with this paper.

Online content
Any methods, additional references, Nature Research reporting summaries, source data, extended data, supplementary information, acknowledgements, peer review information; details of author contributions and competing interests; and statements of data and code availability are available at https://doi.org/10.1038/s41565-020-00782-3.

Competing interests
The authors declare no competing financial interests.

Supplementary information is available for this paper at https://doi.org/10.1038/s41565–020-00782–3.

Peer review information Nature Nanotechnology thanks Rona Chandrawati, Bartosz Grzybowski, Jeffrey Hubbell and the other, anonymous, reviewer(s) for their contribution to the peer review of this work.

Author Manuscript Author Manuscript Author Manuscript Author Manuscript

Abstract

Cancer vaccines hold great promise for improved cancer treatment. However, endosomal trapping and low immunogenicity of tumour antigens usually limit the efficiency of vaccination strategies. Here, we present a proton-driven nanotransformer-based vaccine, comprising a polymer-peptide conjugate-based nanotransformer and loaded antigenic peptide. The nanotransformer-based vaccine induces a strong immune response without substantial systemic toxicity. In the acidic endosomal environment, the nanotransformer-based vaccine undergoes a dramatic morphological change from nanospheres (about 100 nanometres in diameter) into nanosheets (several micrometres in length or width), which mechanically disrupts the endosomal membrane and directly delivers the antigenic peptide into the cytoplasm. The re-assembled nanosheets also boost tumour immunity via activation of specific inflammation pathways. The nanotransformer-based vaccine effectively inhibits tumour growth in the B16F10-OVA and human papilloma virus-E6/E7 tumour models in mice. Moreover, combining the nanotransformer-based vaccine with anti-PD-L1 antibodies results in over 83 days of survival and in about half of the mice produces complete tumour regression in the B16F10 model. This proton-driven transformable nanovaccine offers a robust and safe strategy for cancer immunotherapy.

Cancer vaccines that aim to stimulate tumour-specific immunity hold promise for tumour treatment[1–4]. Cytosolic delivery of appropriate tumour antigens, stimulation of the innate immune system, and cross-presentation of tumour antigens by antigen-presenting cells are essential for inducing strong tumour-specific immunity[1,5]. Nanocarrier systems are promising non-viral agents with which to facilitate cytosolic delivery of many different cargos. Strategies including the use of ‘proton sponge’ polymers[6,7], cell-penetrating peptides[8–10], charge-reversible molecules[11–13] and pore-formation molecules[14–17] have been developed to promote the cytosolic delivery of vaccines[18–20]. In addition, co-delivery of a tumour antigen and an adjuvant in a single nanoparticle has been achieved to boost the poor immunogenicity of the tumour antigen[21–23]. Despite these advances in the field, development of highly efficient antitumour vaccines—especially personalized vaccines that can potently induce T cell priming in humans—is still a challenge[24,25].

Here we report on a proton-driven nanotransformer-based vaccine (NTV) (Fig. 1). The NTV is comprised of a polymer-peptide conjugate-based nanotransformer (NT), along with a loaded antigenic peptide (AP). In acidic media, the particles transform into bigger structures, which causes endosomal membrane disruption and thus cytosolic delivery of the AP. Endosomal membrane integrity and dendritic cell (DC) maturation were analysed after NTV treatment in vitro. Lymph-node-trafficking of NTV and the elicitation of tumour-specific $CD8^+$ T-cells were investigated in vivo. OT-I mice were used to evaluate the antigen-specific T-cell proliferation in vivo. An in vivo killing assay was also exploited to assess the antigen-specific killing induced by the vaccine. The antitumour efficiency of NTV was evaluated in three tumour models (B16F10-OVA, the human papillomavirus (HPV)-E6/E7 tumour model and the B16F10 neoantigen model). Finally, we investigated the effect of combined administration of the neoantigen-loaded NT with anti-PD-L1. All these experiments reveal that the proton-driven transformable nanovaccine induces a robust and safe antitumour immunity.

Author Manuscript Author Manuscript Author Manuscript Author Manuscript

Synthesis and characterization of the NTV

A schematic illustration of the synthesis of a representative NT is shown in Fig. 1a,b and Supplementary Fig. 1. p(DMAEMA$_{22}$-OGEMA$_4$)-*b*-p(MAVE)$_{30}$ was synthesized using reversible addition-fragmentation chain transfer polymerization[26] (Supplementary Fig. 2). Naphthalene-conjugated D-peptide (NDP) forms nanofibres in cells[27]. We found that when naphthalene was replaced with pyrene to give pyrene-conjugated D-peptide (PDP), we obtained nanosheets in water (Supplementary Fig. 3 and 4). This may be because PDP has a larger aromatic structure than the NDP, which may induce stronger **π**-**π** stacking interactions among molecules. We then developed two kinds of NT based on NDP and PDP. Different amounts of hydroxylated NDP (NDP-OH) or hydroxylated PDP (PDP-OH) (Supplementary Figs. 5 and 6) were conjugated to the hydroxyl groups of the p(DMAEMA$_{22}$-OGEMA$_4$)-*b*-p(MAVE)$_{30}$ via an acetal bond (Supplementary Figs. 7–9)[28]. These amphiphilic polymer-peptide conjugates self-assembled into spherical nanostructures at pH 7.4 (Supplementary Figs. 10 and 11). However, an acidic environment (pH 5.6) caused rapid cleavage of the acetal bond and release of the peptides. The released NDP and PDP peptides reassembled into nanofibres and nanosheets, respectively (Supplementary Figs. 10 and 11). After carefully monitoring the size and morphology of these polymer-peptide conjugates at pH 7.4 and pH 5.6 using transmission electron microscopy (TEM) (Supplementary Figs. 10 and 11), we chose p(DMAEMA$_{22}$-OGEMA$_4$)-*b*-p((MAVE)$_{16}$-(MAVE-NDP)$_{14}$) and p(DMAEMA$_{22}$-OGEMA$_4$)-*b*-p((MAVE)$_{18}$-((MAVE-PDP)$_{12}$) to be the NTs representing the 'sphere-to-nanofibre' (nanotransformer 1, NT1) and 'sphere-to-nanosheet' (nanotransformer 2, NT2) types, respectively. TEM and dynamic laser scattering analysis showed that these particles were about 100 nm in diameter and stable when stored at 4 °C (Supplementary Table 2). As controls, we synthesized p(DMAEMA$_{22}$-OGEMA$_4$)-*b*-p((MA)$_{15}$-(MA-NDP)$_{15}$) (NR1) and p(DMAEMA$_{22}$-OGEMA$_4$)-*b*-p((MA)$_{16}$-(MA-PDP)$_{14}$) (NR2) conjugated with pH-unresponsive ester bonds (Supplementary Fig. 12). The proton-driven transformable nature of the NTs inspired us to develop nanocarriers to deliver an AP directly into the cytoplasm via mechanical disruption of the endosomal membrane.

First, we selected a chicken ovalbumin protein-derived peptide (OVA$_{241–270}$) as the model AP (unless noted, all APs mentioned in this study refer to OVA$_{241–270}$). AP-loaded pH-unresponsive NR1 or NR2 nanoparticles (namely NRV1 and NRV2, respectively), and AP-loaded NT1 or NT2 nanoparticles (namely NTV1 and NTV2, respectively) were prepared using a double emulsion method (Fig. 2a, Methods and Supplementary Table 1)[29]. TEM analysis confirmed the pH-dependent transformable nature of NTV1 and NTV2 (Fig. 2b–e). No specific interactions exist between the polymer and the AP (Supplementary Fig. 13). Further investigation of the stiffness of the re-assembled nanostructures revealed that the nanofibres and nanosheets have a high Young's modulus of about 414.4 and 491.1 MPa, respectively (Fig. 2f and Supplementary Fig. 14) in a mimic endosomal environment (pH 5.6). This indicates the high potential of these transformable nanostructures to disrupt endosomal membranes (with resting tension of around 0.06 mN m^{-1} and with a bending rigidity of about 5.2 $k_B T$, where k_B is Boltzmann's constant and T is temperature)[30]. A dye-release experiment was employed to further investigate the ability of these NTs to disrupt endosomal membranes[16]. Figure 2g, h shows that both NTV1 and NTV2 promoted the

Author Manuscript Author Manuscript Author Manuscript Author Manuscript

release of dye from mimic artificial endosomes (AEs) at pH 5.6, while free AP, NRV1 or NRV2 elicited much less dye release under the same conditions. However, all these nanoparticles induced negligible dye release from AEs at pH 7.4. TEM experiments also confirmed the time-dependent disruption of AEs by NTV1 and NTV2 in pH 5.6. NTV2 showed effective disruption of AEs; the AEs were broken into pieces and the large re-assembled nanosheets can be observed in Supplementary Fig. 15. However, although NTV1 also induced AE disruption (small pieces of AE can be observed in Supplementary Fig. 15), most of the reassembled nanostructure was trapped in the AEs, only very few nanofibre structures can be observed under TEM. These results demonstrated that NTV1 and NTV2 have the potential to disrupt endosomal membranes and then release their cargo into the cytoplasm.

NTV2 induces strong and sustained antigen cross-presentation

The release of the AP from the nanoformulations was evaluated using high-performance liquid chromatography (HPLC). As shown in Supplementary Fig. 16, the AP showed sustained release from the nanovaccine in a mimic endosomal acidic environment (pH 5.6); over 80% of the peptide was released in 24 h. All the formulations are endotoxin-free (Supplementary Fig. 17) and non-toxic to bone-marrow-derived dendritic cells (BMDCs), human DCs and two normal cell lines, NIH3T3 and HUVEC cells (Supplementary Fig. 18). We then performed a cellular distribution experiments. As shown in Fig. 3a and Supplementary Fig. 19a–c, compared with free AP (quantification in Supplementary Fig. 19a followed the method of ref.[31]), both NTV1 and NTV2 induced substantial enhancement of the cytosolic peptide fluorescence signal. However, in the chloroquine, NH_4Cl or bafilomycin A1-pre-treatment groups (which increase the pH in the endosome)[32,33], most of the $OVA_{241–270}$-FITC (where FITC is fluorescein isothiocyanate) was located in the endosome, and little fluorescence signal was observed in the cytoplasm (Supplementary Fig. 20a,b), which means that the enhancement of the endosomal pH reverses the cytosolic delivery capacity of the NTVs. However, an acidic liposome (which decreases the pH value in the endosome) pre-treatment enhanced NTV2-induced cytosolic delivery (Supplementary Fig. 20a,b). We found that NTV2-induced cytosolic delivery of AP was a time-dependent process (Supplementary Fig. 20c). We also found that NTV2 induced more surface presentation of AP than free AP, NRV1, NRV2 or NTV1 after 24 h, as determined by staining the $SIINFEKL^{-}H\text{-}2K^{b}$ complexes on the surface of DCs with a specific antibody (Fig. 3b). We also found that DCs treated with free $OVA_{241–270}$ presented very low levels of SIINFEKL at different time points (Supplementary Fig. 21a). The NTV1-treated DCs showed weak surface presentation of the SIINFEKL epitope peptide after 24 h (Supplementary Fig. 21b). In contrast, the cells treated with NTV2 demonstrated a much higher increase in the level of $SIINFEKL^{-}H\text{-}2K^{b}$ complex than cells treated with free AP at 24 h, and this difference remained high even at 48 h (Supplementary Fig. 21c,d).

We next investigated the mechanism of NTV2 uptake and antigen processing. Endocytosis inhibitor assays (Supplementary Fig. 22) showed that NTV2 was internalized by BMDCs mainly via a clathrin-mediated endocytosis process, which means that the nanoparticles are located in endosomes/lysosomes after uptake. We further checked the late endosomal/lysosomal membrane integrity in DC2.4 cells using acridine orange staining[34,35]

Author Manuscript Author Manuscript Author Manuscript Author Manuscript

(Supplementary Fig. 23), galectin puncta assay[36] (Supplementary Fig. 24) and Bio-TEM (Supplementary Fig. 25). These revealed that the endosomal membrane permeation was greatly enhanced after 24 h of NTV2 treatment. These results demonstrate that NTV2 can facilitate sustained delivery of high levels of AP into the cytosol by disrupting the endosome membrane in DC2.4 cells.

We also found that NTV2 potently stimulated the maturation of BMDCs by enhancing the expression levels of cytokines (IL⁻1β, TNF-α, IL⁻10 and IL-12p70) (Fig. 3c, d and Supplementary Fig. 26a,b) and DC-maturing markers such as CD40, CD80 and CD86 (Supplementary Fig. 26c–h). In order to investigate the effect of prolonged AP presence and DC maturation on cross-presentation of AP to T cells, BMDCs were treated with various formulations for 4 h. Next we co-cultured them with OT-I cells for 72 h and then the OT-I cell proliferation level was examined[37]. As shown in Fig. 3e,f, free AP treatment induced limited OT-I cell proliferation in vitro. However, about 80% OT-I cell expansion was observed when the BMDCs were treated with NTV2. But the anti⁻H2K^b-SIINFEKL antibody strongly reversed the T-cell expansion effect (Fig. 3f). Moreover, a CSFE dilution assay (Supplementary Fig. 27) further demonstrated that NTV2 induced much higher OT-I cell proliferation than that of free AP or a positive control of AP + CpG in vivo. But a MHC class-II restricted peptide (OVA$_{317–347}$) delivery using NTV2 was not as efficient (Supplementary Fig. 28). Together, these results indicate that NTV2 delivered the AP efficiently into the cytosol and promoted proliferation of DCs, thereby facilitating prolonged surface presentation of the peptide and cross-presentation to CD8$^+$ T-cells in vitro.

Many studies have shown that combining adjuvants with antigens greatly promotes antigen processing in DCs[38–40]. However, NTV2 facilitated maturation of DCs even in the absence of adjuvants. Recent studies revealed that many nano/microcrystals[41,42] or peptide assemblies[43] activate the NLRP3-inflammasome pathway in the cytoplasm. The morphological similarity between the reassembled nanosheets and the previously published crystals or peptide assemblies prompted us to speculate that the NTV2-induced BMDC maturation may occur via activation of the NLRP3 inflammasome pathway. We then investigated the effects of NTV2 on caspase-1 cleavage and IL-18 release, which are hallmarks of inflammasome formation[44,45] (Supplementary Fig. 29). We found that both NT2 and NTV2 induced significantly increased activation of caspase-1 and IL-18 in BMDCs, whereas free AP and undeformable nanoparticles had limited effect (Supplementary Fig. 29a,b). Minimal caspase-1 cleavage and IL-18 release were observed after NTV1 treatment; however, small interfering RNA (siRNA) to NLRP3 (si-NLRP3) reversed both caspase-1 cleavage and IL⁻18 release in BMDCs, and time-dependent NLRP3 activation was also observed in human DCs. These results demonstrate that NTV2 activates the NLRP3-inflammasome pathway and enhances antigen processing in DCs (Supplementary Fig. 29a,b).

NTV2 effectively delivers aP to lymph nodes

We next tested the effect of NTV2 on the transportation of AP to draining lymph nodes and elicitation of tumour-specific CD8$^+$ T-cell responses in vivo. NTV2 caused negligible lysis of red blood cells at concentrations as high as 500 μg ml^{-1} (Supplementary Fig. 30). Free

Author Manuscript Author Manuscript Author Manuscript Author Manuscript

$OVA_{241–270}$-Cy5.5 or $OVA_{241–270}$-Cy5.5-loaded formulations were injected subcutaneously into C57BL/6 mice at the tail base (equivalent 5 μg peptide per mouse) and the fluorescence intensity of the inguinal lymph nodes was examined 24 h later. Free $OVA_{241–270}$-Cy5.5 resulted in minimal lymph node weight enhancement (Fig. 4b) and only basal Cy5.5 fluorescence was detected in the lymph nodes (Fig. 4c); this may be because of non-specific AP binding at the injection site. In contrast, the lymph node weight was significantly improved (Fig. 4b) and the fluorescence was very high in draining lymph nodes from NTV2-treated mice (Fig. 4a,c). We also found that the NTV2 delivered AP mainly located in antigen-presenting cells like DCs and macrophages (Fig. 4d). The high efficient transportation of lymph nodes may be a result of the potent NLRP3-inflammasome pathway activation. These results demonstrate that NTV2 promotes AP delivery to draining lymph nodes.

Next, we vaccinated C57BL/6 mice three times at 1-week intervals with various formulations. 24 h after the final immunization, the proportion of SIINFEKL-MHC-I tetramer$^+$ CD8$^+$ T-cells in peripheral blood total lymphocytes was determined by flow cytometer (Supplementary Fig. 31a–d). After three injections, the proportion of antigen-specific cytotoxic lymphocytes was extremely low with AP and NT2, but was about 5.8% with NTV2 (Supplementary Fig. 31a,b). As a benchmark comparison, immunization of animals at the same time with the equivalent dose of a mixture of AP and CpG adjuvant (5 μg AP and 50 μg CpG; ref.[2]) elicited ~2.0% antigen-specific cytotoxic lymphocytes (Supplementary Fig. 31a,b, gated in peripheral blood total lymphocytes). We also observed a time-dependent enhancement of the antigen-specific CD8$^+$ T-cell response in NTV2-treated mice after three re-stimulations (7, 14 or 21 days; Supplementary Fig. 31c,d). Also, enhanced granzyme B and IFN-γ[46,47] by the splenocytes were also observed in NTV2-treated mice (Fig. 4e, f). Moreover, an in vivo killing assay (Fig. 4g–o) showed that free $OVA_{241–270}$ induced limited antigen-specific killing in mice, and the AP + CpG DNA mixture elicited about 31.3% antigen-specific killing (for gating strategy, see Supplementary Fig. 32). However, the NTV2 nanovaccine showed about 87.3% antigen-specific killing in vivo. These results demonstrate that the NTV2 nanovaccine elicits strong tumour-specific immune response in vivo.

NTV2 inhibits tumour growth and prolongs survival in tumour-bearing mice

From the various characteristics of NTV2, such as cytosolic delivery, NLRP3-inflammasome activation and potent cross-presentation (Fig. 5a), we evaluated the antitumour efficiency of NTV2 in in vivo tumour models. First, we used the B16F10-OVA melanoma model, in which mice are implanted with B16F10 cells that stably express OVA protein. The model was established by implantation of 1×10^6 B16F10-OVA cells into the right flank of mice at day 0. Various $OVA_{241–270}$-loaded formulations were subcutaneously administered at day 8, followed by two booster shots at day 15 and day 22 (Fig. 5b). The control group received phosphate-buffered sulphate (PBS). Mice body weights were maintained in the normal range during the experimental period (Supplementary Fig. 33), suggesting that no systemic toxicity was induced by NTV2 treatment. In the PBS-treated group, all the tumours reached sizes of 1,500 mm^3 and the mice were killed (after day 23). Free AP, NT2 and NRV2 did not provide any significant tumour growth suppression or animal survival benefit compared with

Author Manuscript Author Manuscript Author Manuscript Author Manuscript

the PBS control (Fig. 5c,d, Supplementary Fig. 33). The NTV1 and positive control AP + CpG induced moderate tumour growth inhibition. Surprisingly, NTV2 resulted in strong tumour growth inhibition, with 37.5% of animals surviving at day 62. To investigate the mechanism under tumour growth inhibition, we performed another animal study to analyse the T-cell infiltration in the tumour tissue at day 23 using a flow cytometer (for gate strategies, see Supplementary Fig. 34). As shown in Fig. 5e, the PBS-treated group showed only about 0.96% total T-cell ($CD45^+CD3^+$) infiltration in the tumour tissue. However, in the NTV2-treated group the T-cell infiltration was 4.8% (Fig. 5e); the total T-cell number increased by about 5 times. The NTV2-treated group showed a significantly higher $CD3^+CD8^+$ to $CD3^+CD4^+$ T-cell ratio in the tumour microenvironment than that of the PBS-treated group (Fig. 5f). Moreover, NTV2 treatment also enhanced the central-memory (CM, defined as $CD45^+CD3^+CD4^+CD44^+CD62L^+$ or $CD45^+CD3^+$ $CD8^+CD44^+CD62L^+$) and effector-memory (EM, defined as $CD45^+CD3^+CD4^+CD44^+CD62L^-$ or $CD45^+CD3^+CD8^+CD44^+CD62L^-$) T-cell populations in the tumour tissue, respectively (Fig. 5g,h). Moreover, a decreased population of regulatory T (Treg) cells ($CD45^+CD3^+CD4^+CD25^+FOXP3^+$) was also found in the tumour tissue in NTV2-treated mice (Fig. 5i). We also checked the expression of the exhaustion marker PD-1 on the $CD45^+CD3^+$ T-cell surface and found that NTV2 treatment also greatly decreased the expression of PD-1 on these cells (Fig. 5j). These results demonstrate that NTV2 resulted in improved total T-cell infiltration, enhanced EM and CM populations in T cells and simultaneously decreased Treg population and the expression of exhaustion marker PD-1, thus providing effective tumour-growth suppression in vivo. We further challenged the vaccinated mice with intravenous injection of tumour cells in vivo (Supplementary Fig. 35). Vaccination with $OVA_{241–270}$-loaded NTV2 almost completely prevented the formation of B16F10-OVA-derived lung nodules. These results demonstrate that NTV2 successfully induced long-term antitumour immunity in the animals. In order to further demonstrate that the NTV2-induced antitumour immunity was mediated by NLRP3-inflammation pathway activation, we constructed a NLRP3 knock-out (NLRP3−/−) mouse model. As shown in Supplementary Fig. 36, NTV2 showed substantial inhibition of tumour growth in wild-type NLRP3+/+ mice. However, the antitumour ability was greatly blunted in NLRP3−/− mice. These results demonstrate that the mechanism of DCs activation in vivo is the NLRP3-inflammasome pathway activation.

To further verify the antitumour efficiency of NTV2, we conducted tests on the HPV E6/7 (TC-1) tumour model. NTV2 was formulated using NT2 as the carrier and an E7-derived peptide ($E7_{43–62}$) as the AP. Mice were injected three times with various formulations at 7-day intervals. In this model, the NTV2-treated animals showed significant tumour growth suppression and 37.5% of the mice had survived at day 83 after tumour inoculation (Fig. 5k, l and Supplementary Fig. 37). Moreover, NTV2 treatment substantially enhanced T-cell infiltration in the tumour microenvironment (Fig. 5m). These data provide further evidence that NTV2 induces tumour-specific immunity, which successfully inhibits tumour growth and prolongs animal survival in vivo.

Given that delivering mutation-derived neoantigens for personalized cancer vaccination is both promising and challenging[48,49], we then tested whether NT2 can be used to deliver neoantigen-based antigen peptide for personalized vaccination in a B16F10 model.

Author Manuscript Author Manuscript Author Manuscript Author Manuscript

Mutation-derived neoantigen peptides[50] (mixture of B16-M27, B16-M30, B16-M47 and B16-M48) were used as antigens in the vaccines. No obvious decrease in the mice body weight was detected during vaccine treatment (Fig. 6a), indicating the bio-compatibility of the vaccines. Our results showed that APs alone or NRV2 vaccination induced limited tumour growth inhibition in the B16F10 model (Fig. 6b). Although NTV1 and CpG + APs showed inhibition of tumour growth at day 32, the tumours continued to grow bigger when the three vaccinations were over (Fig. 6e). However, NTV2 nanovaccine treatment significantly inhibited tumour growth and prolonged animal survival (Fig. 6c–e). Although the NTV2 alone cannot induce a complete response in the neoantigen model, combination treatment with the neoantigen nanovaccine and anti-PD-L1 showed the most effective antitumour efficiency (Fig. 6b,d). Half of the mice were tumour-free or without detectable tumour foci after the combination treatment at day 83 (Fig. 6e). We also found significant enhancement of $CD45^+CD3^+$ T-cell infiltration (Fig. 6f), a higher $CD45^+CD3^+CD8^+$ to $CD45^+CD3^+CD4^+$ ratio (Fig. 6g and Supplementary Fig. 38) in the NTV2 + anti-PD-L1 group, and improved populations of $CD44^+CD62L^+$ CM T cells and the $CD44^+CD62L^-$ EM T cells in $CD45^+CD3^+CD4^+$ T cells and $CD45^+CD3^+CD8^+$ T cells were also observed (Fig. 6h,i) in the combination therapy group. We also found the NTV2 + anti-PD-L1 treatment induced a decreased infiltration of Treg cells compared to PBS or other formulations (Fig. 6j). Finally, the decreased exhaustion marker PD-1 on the T-cell surface was detected in the combination treatment group (Fig. 6k). These results demonstrate that NTV2 combined with antibody to PD-L1 induced potent antitumour immune response in the neoantigen tumour model. We further performed a tumour cell re-challenging experiment in the tumour-free mice, as shown in Supplementary Fig. 39; B16F10 cells can hardly grow in the tumour-free mice, whereas saline-treated mice showed a fast growth of tumour. These results demonstrate that the NT-based platform is a potential tool for personalized cancer immunotherapy in the future.

Moreover, mice receiving the NTV2 showed much lower systemic levels of cytokines (IL-1β, IL-12p70, IL-6, IFN-γ and TNF-α) than mice treated with CpG (Supplementary Fig. 40). This suggests that the combinational therapy induces no, or very low, systemic toxicity. Further histological analysis did not reveal any observable toxicity in the major organs (heart, liver, lung, spleen and kidney) in vaccinated mice (Supplementary Fig. 41,42). Moreover, the blood biochemistry assay shown in Supplementary Table 3 reveals that the alanine transaminase, aspartate transaminase, blood urea nitrogen and creatinine kept in the normal range compared with PBS-treated mice. These results demonstrate that NTV2 is biompatible and safe for future personalized vaccination delivery.

Conclusions

In summary, we have developed a proton-driven transformable nanovaccine that not only facilitates cytosolic delivery and cross-presentation of APs, but also activates the NLRP3-inflammasome pathway and thus boosts antitumour immunity. We show that the NTs enhance the presentation of both model antigens and tumour neoantigens by DCs, which causes a more-robust stimulation of $CD8^+$ T cells. Also, combinational treatment of the neoantigen vaccine with anti-PD-L1 induced significant inhibition of tumour growth and prolonged animal survival. The NT-based carriers can easily be adapted to encapsulate

Author Manuscript Author Manuscript Author Manuscript Author Manuscript

tumour neoantigens or used for combined administration with other checkpoint blockades or therapeutics. We predict that these characteristics of NTV2 will facilitate its use in the prevention and treatment of many infectious diseases when loaded with pathogenic antigens.

Methods

Chemicals.

Piperidine, anisole, thioanisole, 1,2-ethanedithiol, *N*,*N*-diisopropylethylamine (DIEA), 1–1H-1,2,3-triazolopyridinium 3-oxid hexafluorophosphate (HATU), 2-naphthaleneacetic acid, 1-pyreneacetic acid, trifluoroacetic acid (TFA), RAFT CTA 4-cyanopentanoic acid dithio-benzoate (CPADB), 2,2-azobisisobutyronitrile (AIBN), 2-(dimethylamino)ethyl methacrylate (DMAEMA), ethanolamine, methacrylic acid (MAA), 1,1'-carbonyldiimidazole (CDI), 1-palmitoyl-2-stearoyl-sn-glycero-3-phosphocholine (HSPC), 2-chloroethyl vinyl ether, *p*-toluene sulphonic acid (p-TSA) and oligo(ethylene glycol) monomethyl ether methacrylate (OEGMA, number-average molecular weight (Mn) = 300 and 4~5 pendant ethylene oxide units) were purchased from Sigma-Aldrich. The ovalbumin antigenic long peptide $OVA_{241–270}$ (SMLVLLPDEVSGLEQLESIINFEKLTEWTS) (contains MHC I epitope peptide), $OVA_{317–347}$ (SSAESLKISQAVHAAHAEINEAGREVVGSAE) (contains MHC II epitope peptide), the human papillomavirus antigenic peptide (HPV $E7_{43–62}$, GQAEPDRAHYNIVTFCCKCD) and B16 neoantigen peptides (B16-M27, REGVELCPGNKYEMRRHGTTHSLVIHD; B16-M30, PSKPSFQEFVDWENV SPELNSTDQPFL; B16-M47, GRGHLLGRLAAIVGKQVLLGRKVVVVR; B16-M48, SHCHWNDLAVIPAGVVHNWDFEPRKVS) were purchased from Shanghai Top Biotechnology (Shanghai, China). Antibodies against mouse H-2Kb bound to SIINFEKL (anti-mouse H-2Kb bound to SIINFEKL, catalogue number (cat. no.) 141603), anti-CD45-Pacific blue (cat. no. 103125), anti-CD3-PE (cat. no. 100312), anti-CD4-FITC (cat. no. 100510), anti-CD8-APC (cat. no. 100712), anti-CD44-PE/Cy7 (cat. no. 103029), anti-CD62L-Percp-Cy5.5 (cat. no. 104431), anti-PD-1-APC (cat. no. 135209), anti-CD25-PE/cy7 (cat. no. 101915) anti-CD80-APC (cat. no.104713), anti-CD86-APC (cat. no.105011) and anti-CD40-APC (cat. no.124611) were purchased from Biolegend (San Diego, USA). Anti-Foxp3-Percp-Cy5.5 (cat. no. 563902) was obtained from BD Pharmingen. PE-conjugated H-2Kb/OVA (SIINFEKL) tetramer (cat. no. TB-5001–1) was obtained from Medical and Biological Laboratories Co. Ltd. For all the flow experiments, antibodies were diluted 200 times before use. Anti-PD-L1 (cat. no. BP0101) was obtained from BioXcell. Mouse cytokine ELISA kits for IL-1β (cat. no. BMS224HS), IL-6 (cat. no. KMC0061), IL-12p70 (cat. no. EMIL12B), TNF-α (cat. no. KMC3012), IFN-γ (cat. no. BMS609TEN) and Granzyme B (cat. no. 88-8022-22) were purchased from Invitrogen. siRNA targeting NLRP3 were purchased from GenePharma Corp. (Shanghai, China).

Cell lines and animals.

The TC-1 tumour cell line co-transfected with the HPV-16 oncoproteins E6 and E7 and the c-Ha-*ras* oncogene was obtained from the Tumour Center of the Chinese Academy of Medical Sciences. The DC2.4 cell line was a gift from H. Wang. B16F10 cells transfected to express chicken OVA (B16F10-OVA cells) were a gift from C. Xu. All the cell lines were

Author Manuscript Author Manuscript Author Manuscript Author Manuscript

authenticated by a short tandem repeat DNA profiling method and no mycoplasma contamination was detected in the above cell lines. Female C57BL/6 mice (6–8 weeks) were purchased from Vital River Laboratory Animal Technology Co. Ltd. (Beijing, China). OT-I and OT-II transgenic mice were from M. Zhu (Institute of Biophysics, Chinese Academy of Sciences). NLRP3−/− mice on a C57BL/6 background with 7-base-pair deficiency at the promoter region of Nlrp3 were donated by H. Liu from Changzheng Hospital, Shanghai. Mice were housed in a specific-pathogen-free animal facility at ambient temperature (22 ± 2 °C), air humidity 40%–70% and 12-h dark/12-h light cycle.

Generation of BMDCs.

BMDCs were isolated[51] from the femurs and tibias of 6-week-old female C57BL/6 mice and cultured in RPMI 1640 medium containing 10% fetal bovine serum, 10 ng ml^{-1} IL-4 and 50 ng ml^{-1} recombinant mouse granulocyte/macrophage colony-stimulating factor at 37 °C for 6 days. Immature DCs were then harvested. The culture medium was changed every 2 days. Usually, 4×10^6 immature DCs were obtained from each mouse.

Synthesis of peptides.

NDP and PDP peptides were synthesized by a solid-phase strategy. 20% (v/v) piperidine was used to deprotect Fmoc groups on the amino-terminals of the peptides. DIEA (0.4 M) and HATU in anhydrous DMF were used to activate the carboxy-terminal amino acid. Cleavage of peptides from the resin was performed using a mixture of TFA (95% v/v), thioanisole (5% v/v), anisole (2% v/v), and 1,2-ethanedithiol (3% v/v) for 2 h. Crude peptides were purified by preparative HPLC.

Synthesis of p(OEGMA$_4$-DMAEMA$_{22}$).

The general synthetic process is as follows. DMAEMA (1.35 g, 8.6 mmol), OEGMA (0.5 g, 1.77 mmol), CPADB (40 mg, 0.15 mmol) and AIBN (4.8 mg, 0.029 mmol) were dissolved in 5 ml dry DMF in sealed tubes. After three freeze-evacuate-thaw cycles and then sealing, the tubes were immersed in a 60 °C oil bath with magnetic stirring for 18 h. Quenching of the polymerization was carried out by immersing the tube in a bottle containing liquid nitrogen. After thawing, the solution was dialysed against water and then lyophilized. Yield was 90%. The average molecular weight and polydispersity were determined using ^{1}H-nuclear magnetic resonance spectroscopy (NMR) (with MestReNova 9.0 soft well) and gel permeation chromatography, respectively.

Synthesis of p(OEGMA$_4$-DMAEMA$_{22}$)-*b*-p(MA$_{30}$).

Block copolymer p(OEGM A$_4$-DMAEMA$_{22}$)-*b*-p(MA$_{30}$) was prepared using p(OEGMA$_4$-DMAEMA$_{22}$) as the macromolecular chain transfer agent (macroCTA). p(OEGMA$_4$-DMAEMA$_{22}$) (550 mg, 0.1 mmol), MA (1.7 g, 20 mmol) and 3.28 mg AIBN (0.02 mmol) were first dissolved in 5 ml dry DMF. After three freeze-evacuate-thaw cycles, the tube was immersed in a 60 °C oil bath. After another 0.5 h, the reaction was quenched using liquid nitrogen. The polymer was purified by dialysis against pure water for 48 h. Yield was 65%. The average molecular weight and polydispersity were determined using ^{1}H-NMR and gel permeation chromatography, respectively.

Author Manuscript Author Manuscript Author Manuscript Author Manuscript

Synthesis of p(OEGMA$_4$-DMAEMA$_{22}$)-*b*-p((MAVE)$_{16}$-(MAVE-NDP)$_{14}$).

Conjugation of NDP-OH with p(OEGMA$_4$-DMAEMA$_{22}$)-b-p(MA$_{30}$) was carried out following a method described previously[28]. First, vinyl ether of p(OEGMA$_4$-DMAEMA$_{22}$)-b-p(MA$_{30}$) was obtained following ref.[28]. Dry DMF (20 ml) containing p(OEGMA$_4$-DMAEMA$_{22}$)-*b*-p(MA$_{30}$) (2.4 g, 10 mmol of carboxyl group) and KOH (1 g, 17.8 mmol) was added to a 100 ml flask with gentle stirring under an N_2 atmosphere. Then a mixture of 2-chloroethyl vinyl ether (2.1 g, 20 mmol) in anhydrous DMF (10 ml) was added. After 24 h, the mixture was dialysed against ultrapure water for 48 h and finally the vinyl ether of p(OEGMA$_4$-DMAEMA$_{22}$)-*b*-p(MAVE$_{30}$) were collected by lyophilization. The as-obtained product was characterized using ^{1}H-NMR.

The procedure for conjugating NDP-OH with p(OEGMA$_4$-DMAEMA$_{22}$)-*b*-p(MAVE$_{30}$) to obtain p(OEGMA$_4$-DMAEMA$_{22}$)-*b*-p((MAVE)$_x$-(MAVE-NDP)$_y$) ($x + y = 30$) is exemplified by the synthesis of p(OEGMA$_4$-DMAEMA$_{22}$)-*b*-p((MAVE)$_{16}$-(MAVE-NDP)$_{14}$). Dry DMF (25 ml) was added to a 100 ml flask containing 0.35 g p(OEGMA$_4$-DMAEMA$_{22}$)-*b*-p(MAVE$_{30}$) (1 mmol vinyl ether), 44 mmol p-TSA and 4 Å molecular sieve (1 g) under an N_2 atmosphere. Then, 0.7 mmol NDP-OH was added and the reaction was kept at 60 °C. After 48 h, the mixture was concentrated in a vacuum, dialysed against DMF for 24 h and then dialysed against PBS (pH 7.4) for 48 h. The product was finally collected by lyophilization. p(OEGMA$_4$-DMAEMA$_{22}$)-*b*-p((MAVE)$_x$-(MAVE-NDP)$_y$) and p(OEGMA$_4$-DMAEMA$_{22}$)-*b*-p(MAVE-)$_m$-(MAVE-PDP)$_n$ with different peptide conjugate ratios ($x + y = 30$, $m + n = 30$) were obtained by tuning the ratio between p(OEGMA$_4$-DMAEMA$_{22}$)-*b*-p(MAVE$_{30}$) and NDP or PDP.

Preparation of proton-driven NTV.

NTV was obtained using a water-in-oil-in-water double emulsion solvent evaporation method[52]. A solution of 100 μl AP (2.5 mg ml^{-1}) in PBS (internal water phase) was emulsified for 20 s with 1 ml CH_2Cl_2 containing 5 mg polymer-peptide conjugation (oil phase) using a probe sonicator. The as obtained 1st emulsion (water in oil) was added into 10 ml PBS (pH 7.4) solution (external water phase) to produce a double water-in-oil-in-water emulsion. Finally, CH_2Cl_2 was removed under vacuum and the resulting NTV was washed three times with PBS. The resulting nanoparticles were then stored at 4 °C. Fluorescent nanoparticles were prepared by replacing 10% of the peptide with FITC-conjugated peptide, which was synthesized in our laboratory.

pH-sensitive release.

The release of AP from NTV1 or NTV2 was studied using a dialysis bag at 37 °C in acetate buffer (pH 5.6) or PBS (pH 7.4). 10 mg of the nanovaccine was dispersed in acetate buffer or PBS and kept at 37 °C for 24 h. Then the nanoparticles were removed by centrifuge (10,000 rpm, 10 min) at 2 h, 4 h, 6 h, 8 h, 10 h, 12 h, 24 h and 48 h, and the supernatant were collected for HPLC.

Atomic force microscopy.

Nanoindentation was performed using an Agilent 5500 atomic force microscope (California, USA) equipped with an optical microscope (Nikon ECLIPS Ti, Tokyo, Japan). Atomic force

Author Manuscript Author Manuscript Author Manuscript Author Manuscript

microscopy probes used for detection of force curves are Bruker FMV cantilevers (California, US). Cantilever stiffness is about 2.0 N m^{-1} and the tip radius is about 8 nm.

Five milligrams of the NT1 or NT2 were dissolved in an acetate buffer (pH 5.6) for 30 min, spotted on a silicon surface and left until the nanostructures had adsorbed. After another 30 min, substrates were washed several times with acetate buffer to remove the unadsorbed materials. Finally, the samples were immersed in acetate buffer before atomic force microscopy measurements. Before probing, the cantilever was immersed in the buffer for 2 h to reach thermal equilibrium. For each sample, at least three different nanostructures were probed. Approach and retraction force curves were obtained at a constant speed of 10,000 nm s^{-1}. Force versus distance curves were obtained by compressing the nanostructures with the atomic force microscope probe. Young's moduli were extracted using MATLAB 12.0 software.

AP loading efficiency and characterization of nanomaterials.

The loading efficiency of $OVA_{241–270}$ in nanovaccines was determined by HPLC. For nanoparticle characterizations, NTV was diluted to 0.1 mg ml^{-1} with PBS, and the size distributions of the particles were determined by dynamic light scattering. The morphology of the nanomaterials was observed under TEM. Images were obtained on an HT7700 (HATICHI, Japan) or Tecnai G^2 F20 (FEI, USA) system (with digital micrograph3.7 software, https://www.gatan.com/products/tem-analysis/gatan-microscopy-suite-software).

pH-dependent disruption of endosomes evaluated using mimic AEs.

Before using the NTV in vitro and in vivo, the pH-dependent shape transformation and the ability to disrupt the endosome membrane were evaluated using mimic AEs[16]. The fluorophore ANTS and p-xylene-bis (pyridinium) bromide (DPX, quencher) are a fluorophore/quencher pair, which have relatively stable fluorescence at pH values above 4; ref.[53]. ANTS and DPX were encapsulated within AEs to evaluate whether the NTV can disrupt the membrane and induce dye release. AEs were prepared using a two-step method. First, a mixture of methanol and chloroform (1:1) containing POPC/POPG (molar ratio = 3:1) was rotary evaporated to obtain a thin lipid film. The film was dried overnight under vacuum, then hydrated with a solution containing 70 mM NaCl (pH 7.4), 12.5 mM ANTS, 45.0 mM DPX and a certain amount of NTV1 or NTV2. The EAs encapsulating ANTS/DPX/NT were separated from free dyes using a Millipore ultrafiltration device (with molecular weight cut off of 30,000). Lipid concentration was determined using a phosphatidylcholine assay kit.

For the dye-leakage experiment, AEs encapsulating NTV were dissolved in a phosphate buffer (pH 7.4) or in an acetate buffer (pH 5.6) containing 70 mM NaCl at 37 °C. After 30 min, the fluorescence intensities in the mixtures were determined using a HITACHI F-7000 fluorescence spectrophotometer. AEs lysed with 0.5% Triton X-100 was used as the positive control and freshly prepared AEs encapsulating NTV were used as the negative control.

Author Manuscript Author Manuscript Author Manuscript Author Manuscript

Endocytosis inhibition assays.

To investigate the cellular internalization mechanisms of NTV2, an endocytosis inhibition assay was performed. BMDCs were treated with complete culture medium containing the following endocytosis inhibitors: 10 μg ml^{-1} chlorpromazine for inhibition of clathrin-mediated endocytosis; 5 μg ml^{-1} cytochalasin D for inhibition of macropinocytosis-mediated endocytosis; 5 mM methyl-β-cyclodextrin for inhibition of lipid raft-mediated endocytosis; 200 μM genistein for inhibition of caveolae-mediated endocytosis; and 0.1% NaN_3/50 mM 2-deoxyglucose and low temperature (4 °C) for inhibition of energy-dependent endocytosis. After 30 min, the medium was replaced with fresh complete medium containing NTV2 (125 μg ml^{-1}) and the same kind of endocytosis inhibitor for another 30 min. Control cells were treated with complete medium containing 125 μg ml^{-1} NTV2. After that, the medium was discarded and the cells were washed with PBS several times before flow cytometry analysis.

Intracellular distribution.

For intracellular distribution studies, DC2.4 cells were incubated with $OVA_{241–270}$-FITC-loaded nanoparticles or free $OVA_{241–270}$-FITC (at a $OVA_{241–270}$ concentration of 5 μg ml^{-1}) for 24 h. The cells were then washed with PBS and stained with Lysotracker Deep Red and Hoechst 33342 (nuclear staining) for 20 min. After that, fresh medium was added and the intracellular distribution of the nanomaterials was observed under confocal laser scanning microscope (with ZEN 2010 software, https://www.zeiss.com/microscopy/us/products/microscope-software.html).

Cellular late endosomal/lysosomal membrane permeability.

Endosomal membrane permeability in NTV-treated DC2.4 cells was investigated using an acridine orange staining method[34,35]. The loss of endosomal/lysosomal membrane permeability can be measured as a decrease of red fluorescence and simultaneously an increase of green fluorescence[35]. DC2.4 cells were incubated with free AP, NT2 alone or NTV2 with equivalent (AP) 5 μg ml^{-1} for 24 h. Cells were washed with PBS, then incubated with culture medium containing acridine orange (2.5 μg ml^{-1}) for 15 min. The endo/lysosome membrane permeability of DC2.4 cells was then analysed under CLSM with excitation at 488 nm, and emission at 540 nm (green) and 620 nm (red).

Cytokine release from NTV2-treated DCs.

Cytokine levels in the supernatants of cultured BMDCs were determined using mouse IL-1β, and IFN-γ ELISA kits were used according to the protocols supplied by the manufacturer.

Cytokine release and granzyme expression following restimulation of splenocytes with AP.

Seven days after the last immunization, the spleens of mice in various treatment groups were collected and splenocytes were isolated by mincing against a 200-mesh cell strainer. 4×10^6 splenocytes were incubated with SIINFEKL peptide. Release of IFN-γ and Granzyme B from splenocytes was quantified using IFN-γ and Granzyme-B-specific ELISA kits.

Author Manuscript Author Manuscript Author Manuscript Author Manuscript

In vitro OT-I cell proliferation assay.

BMDCs were isolated from C57BL/6 mice and cultured in medium containing IL-4 and granulocyte/macrophage colony-stimulating factor for 7 days before use. BMDCs were incubated with various formulations (at equivalent AP concentration 5 μg ml^{-1}) for 24 h, and then the cells were washed with PBS and mixed at a ratio of 1:10 with OT-I cells that had been stained with 5- (and 6-) carboxyfluorescein diacetate succinimidyl ester (CFSE). After 3 days, proliferation of OT-I cells was assessed by flow.

In vivo OT-I or OT-II cell proliferation assay.

C57BL/6 mice were vaccinated with three times of various formulations (at 7-day intervals). After 7 days after the last vaccination, OT-I/OT-II T cells that were labelled with CFSE (3×10^6 T cells per mouse) were injected into the tail veins of the mice. After 3 days, spleens of mice were isolated and the splenocytes were analysed by flow cytometry.

In vivo killing assay.

C57BL/6 mice were vaccinated (on day 0) via subcutaneous injection into the tail base with various formulations (three times at 7-day intervals). On 7 days after the last vaccination, naive splenocytes (from untreated C57BL/6 mice) were incubated with SIINFEKL peptide (5 μg ml^{-1}) or PBS for 1 h. These were washed with PBS and the SIINFEKL-pulsed cells were labelled with 0.25 μM CFSE and the PBS-treated cells were incubated with 2.5 μM CSFE for 30 min, respectively. Then, 5×10^6 $CFSE^{low}$-and $CFSE^{high}$-labelled cells (in a 1:1 ratio) were injected intravenously into vaccinated mice. After 24 h, the ratio of $CFSE^{high}$- and $CFSE^{low}$-labelled cells remaining in spleen was analysed. The antigen-specific lysis percentage in each treatment group was determined as follows:

$$\text{Lysis}(\%) = 100 - \left[100 \times \left(\%\text{CFSE}^{\text{high}} - \text{vaccinated}/\%\text{CFSE}^{\text{low}} - \text{vaccinated}\right) / \left(\%\text{CFSE}^{\text{high}} - \text{PBS}/\%\text{CFSE}^{\text{low}} - \text{PBS}\right)\right]. \quad (1)$$

Investigation of the mechanism of NTV-induced DC activation.

The levels of active caspase-1 in NTV-treated BMDCs were investigated using a caspase-1 colorimetric assay kit (acetyl-Tyr-Val-Ala-Asp *p*-nitroanilide, cat. no. R20239) that specifically recognises active caspase-1. Briefly, BMDCs were primed with AP alone, NT2 alone and NTV (5 μg ml^{-1} AP) for 5 h. Then the cells were collected and lysed at 4 °C. Then, 2 mM Ac-YVAD-pNA was added and the mixture was kept at 37 °C for 2 h. Finally, absorptions at 410 nm were measured and the data were normalized to BMDC controls.

Lymph node draining.

For lymph-node-draining studies, C57BL/6 mice were subcutaneously injected with PBS, $OVA_{241–270}$-Cy5.5 alone or $OVA_{241–270}$-Cy5.5-loaded NTV2. After 24 h, mice inguinal lymph nodes were isolated, and fluorescence signals in lymph nodes were measured with a Maestro EX-RRO In-Vivo Imaging system.

Author Manuscript Author Manuscript Author Manuscript Author Manuscript

Evaluation of systemic cytokine levels after nanovaccine treatment.

C57BL/6 mice were subcutaneously administered with 125 μg NTV2, 50 μg of CpG or PBS with the same volume. Serum cytokine levels were measured over time by using ELISA kits for IL-1β, IL-12p70, IL-6, IFN-γ and TNF-α.

In vivo vaccination and cancer immunotherapy studies.

All protocols performed on animals in this study were approved by the Ethics Committee of the Institute of Process Engineering, CAS. C57BL/6 mice (female) aged 6–8 weeks ($n = 8$) were subcutaneously injected in the flank with 1×10^6 B16F10-OVA cells or TC-1 cells on day 0. Mice were vaccinated on the indicated days by subcutaneous injection of various formulations with equivalent dose of AP (5 μg ml^{-1}). Tumour size was measured every three days and tumour volume was calculated as $width^2 \times length \times 0.5$. Mice were sacrificed when the tumour size reached 1,500 mm^3 or when animals became moribund with severe weight loss or ulceration. Animal studies were stopped when the experiment reached twice the longest survival time of the saline control. For the tumour cell challenge model, pre-immunized mice were challenged by intravenous injection of B16F10-OVA tumour cells (1.0×10^5 per mouse) on day 0, and lungs were excised on day 15. Lung tumour nodules were then counted.

Statistical analysis.

Sample size was determined by pilot immunization and tumour treatment studies. All statistical differences were calculated using Graphpad prism 7.0 software. Error bars represent means ± standard deviation (s.d.). Animal studies were performed after randomization and with 8 mice in each group. Statistical differences between two groups were determined using two-tailed Student's *t*-test. The Kaplan-Meier method was used to analyse the differences in animal survival and the *P* value was calculated by the log-rank test.

Reporting Summary.

Further information on research design is available in the Nature Research Reporting Summary linked to this article.

Supplementary Material

Refer to Web version on PubMed Central for supplementary material.

Acknowledgements

This work was financially supported by the National Natural Science Foundation of China (grant numbers 31630027, 31430031, 21327806, 21621003 and 21235004) and NSFC-German Research Foundation (DFG) project (grant number 31761133013). We are grateful for support from the Strategic Priority Research Program of the Chinese Academy of Sciences (grant numbers XDA09030301 and XDB36000000), the National Key Research and Development Program of China (grant numbers 2018YFE0117800 and 2016YFA0203101). We also acknowledge support from the NIH/NIMHHD (grant number U54MD007597). We thank Z. Ao for help with the AFM measurements and X. Hu and H. Guo for help with the TEM analysis.

Author Manuscript Author Manuscript Author Manuscript Author Manuscript

References

1. Irvine DJ, Hanson MC, Rakhra K & Tokatlian T Synthetic nanoparticles for vaccines and immunotherapy. Chem. Rev 115, 11109–11146 (2015). [PubMed: 26154342]
2. Kuai R, Ochyl LJ, Bahjat KS, Schwendeman A & Moon JJ Designer vaccine nanodiscs for personalized cancer immunotherapy. Nat. Mater 161, 489–496 (2016).
3. Sahin U et al. Personalized RNA mutanome vaccines mobilize poly-specific therapeutic immunity against cancer. Nature 547, 222–226 (2017). [PubMed: 28678784]
4. Ott PA et al. An immunogenic personal neoantigen vaccine for patients with melanoma. Nature 547, 217–221 (2017). [PubMed: 28678778]
5. Goldberg MS Immunoengineering: how nanotechnology can enhance cancer immunotherapy. Cell 161, 201–204 (2015). [PubMed: 25860604]
6. Chou LY, Ming K & Chan WC Strategies for the intracellular delivery of nanoparticles. Chem. Soc. Rev 40, 233–245 (2011). [PubMed: 20886124]
7. Yin H et al. Non-viral vectors for gene-based therapy. Nat. Rev. Genet 15, 541–555 (2014). [PubMed: 25022906]
8. Douat C et al. A cell-penetrating foldamer with a bioreducible linkage for intracellular delivery of DNA. Angew. Chem. Int. Ed 54, 11133–11137 (2015).
9. D'Astolfo DS et al. Efficient intracellular delivery of native proteins. Cell 161, 674–690 (2015). [PubMed: 25910214]
10. Stewart MP et al. In vitro and ex vivo strategies for intracellular delivery. Nature 538, 183–192 (2016). [PubMed: 27734871]
11. Blanco E, Shen H & Ferrari M Principles of nanoparticle design for overcoming biological barriers to drug delivery. Nat. Biotechnol 33, 941–951 (2015). [PubMed: 26348965]
12. Kanasty R, Dorkin JR, Vegas A & Anderson D Delivery materials for siRNA therapeutics. Nat. Mater 12, 967–977 (2013). [PubMed: 24150415]
13. Luo M et al. A STING-activating nanovaccine for cancer immunotherapy. Nat. Nanotech 12, 648–654 (2017).
14. Cheng Y, Yumul RC & Pun SH Virus-inspired polymer for efficient in vitro and in vivo gene delivery. Angew. Chem. Int. Ed 128, 12192–12196 (2016).
15. Martens TF, Remaut K, Demeester J, De Smedt SC & Braeckmans K Intracellular delivery of nanomaterials: how to catch endosomal escape in the act. Nano Today 9, 344–364 (2014).
16. Akishiba M et al. Cytosolic antibody delivery by lipid-sensitive endosomolytic peptide. Nat. Chem 9, 751–761 (2017). [PubMed: 28754944]
17. Cheng CJ et al. MicroRNA silencing for cancer therapy targeted to the tumour microenvironment. Nature 518, 107–110 (2015). [PubMed: 25409146]
18. Keller S et al. Neutral polymer micelle carriers with pH-responsive, endosome-releasing activity modulate antigen trafficking to enhance CD8+ T cell responses. J. Control. Release 191, 24–33 (2014). [PubMed: 24698946]
19. Shae D et al. Endosomolytic polymersomes increase the activity of cyclic dinucleotide STING agonists to enhance cancer immunotherapy. Nat. Nanotech 14, 269–278 (2019).
20. Wilson JT et al. Enhancement of MHC-I antigen presentation via architectural control of pH-responsive, endosomolytic polymer nanoparticles. AAPS J. 17, 358–369 (2015). [PubMed: 25501498]
21. Xia X et al. Porous silicon microparticle potentiates anti-tumor immunity by enhancing cross-presentation and inducing type interferon response. Cell Rep. 11, 957–966 (2015). [PubMed: 25937283]
22. Morishita M, Takahashi Y, Matsumoto A, Nishikawa M & Takakura Y Exosome-based tumor antigens-adjuvant co-delivery utilizing genetically engineered tumor cell-derived exosomes with immunostimulatory CpG DNA. Biomaterials 111, 55–65 (2016). [PubMed: 27723556]
23. Wilson DS et al. Antigens reversibly conjugated to a polymeric glyco-adjuvant induce protective humoral and cellular immunity. Nat. Mater 18, 175–185 (2019). [PubMed: 30643235]

Author Manuscript Author Manuscript Author Manuscript Author Manuscript

24. Riley RS, June CH, Langer R & Mitchell MJ Delivery technologies for cancer immunotherapy. Nat. Rev. Drug Discov 18, 175–196 (2019). [PubMed: 30622344]
25. Tanyi JL et al. Personalized cancer vaccine effectively mobilizes antitumor T cell immunity in ovarian cancer. Sci. Transl. Med 10, eaao5931 (2018). [PubMed: 29643231]
26. Chiefari J et al. Living free-radical polymerization by reversible addition-fragmentation chain transfer: the RAFT process. Macromolecules 31, 5559–5562 (1998).
27. Zhou J, Du X, Yamagata N & Xu B Enzyme-instructed self-assembly of small d-peptides as a multiple-step process for selectively killing cancer cells. J. Am. Chem. Soc 138, 3813–3823 (2016). [PubMed: 26966844]
28. Zhong Y et al. Hyaluronic acid-shelled acid-activatable paclitaxel prodrug micelles effectively target and treat CD44-overexpressing human breast tumor xenografts in vivo. Biomaterials 84, 250–261 (2016). [PubMed: 26851390]
29. Zambaux M et al. Influence of experimental parameters on the characteristics of poly (lactic acid) nanoparticles prepared by a double emulsion method. J. Control. Release 50, 31–40 (1998). [PubMed: 9685870]
30. Wilhelm C, Cebers A, Bacri J-C & Gazeau F Deformation of intracellular endosomes under a magnetic field. Eur. Biophys. J 32, 655–660 (2003). [PubMed: 12811432]
31. Gong N et al. Carbon-dot-supported atomically dispersed gold as a mitochondrial oxidative stress amplifier for cancer treatment. Nat. Nanotech 14, 379–387 (2019).
32. Qiu L et al. Self-assembled pH-responsive hyaluronic acid-g-poly (l-histidine) copolymer micelles for targeted intracellular delivery of doxorubicin. Acta Biomater. 10, 2024–2035 (2014). [PubMed: 24365705]
33. Alam MM et al. Endogenous inspired biomineral-installed hyaluronan nanoparticles as pH-responsive carrier of methotrexate for rheumatoid arthritis. J. Control. Release 252, 62–72 (2017). [PubMed: 28288894]
34. Zhang Z et al. Mesoporous silica-coated gold nanorods as a light-mediated multifunctional theranostic platform for cancer treatment. Adv. Mater 24, 1418–1423 (2012). [PubMed: 22318874]
35. Petersen NH, Kirkegaard T & Jäättelä M Lysosomal stability assay. Bio Protoc. 4, e1162 (2014).
36. Aits S et al. Sensitive detection of lysosomal membrane permeabilization by lysosomal galectin puncta assay. Autophagy 11, 1408–1424 (2015). [PubMed: 26114578]
37. Goel S et al. CDK4/6 inhibition triggers anti-tumour immunity. Nature 548, 471 (2017). [PubMed: 28813415]
38. Fan Y et al. Immunogenic cell death amplified by co-localized adjuvant delivery for cancer immunotherapy. Nano Lett. 17, 7387–7393 (2017). [PubMed: 29144754]
39. Duan F et al. A simple and powerful co-delivery system based on pH-responsive metal-organic frameworks for enhanced cancer immunotherapy. Biomaterials 122, 23–33 (2017). [PubMed: 28107662]
40. Li AV et al. Generation of effector memory T cell-based mucosal and systemic immunity with pulmonary nanoparticle vaccination. Sci. Transl. Med 5, 204ra130 (2013).
41. Rosenthal AK & Ryan LM Calcium pyrophosphate deposition disease. N. Engl. J. Med 374, 2575–2584 (2016). [PubMed: 27355536]
42. Martinon F, Pétrilli V, Mayor A, Tardivel A & Tschopp J Gout-associated uric acid crystals activate the NALP3 inflammasome. Nature 440, 237–241 (2006). [PubMed: 16407889]
43. Heneka MT et al. NLRP3 is activated in Alzheimer's disease and contributes to pathology in APP/PS1 mice. Nature 493, 674–678 (2013). [PubMed: 23254930]
44. Ghiringhelli F et al. Activation of the NLRP3 inflammasome in dendritic cells induces IL-1β-dependent adaptive immunity against tumors. Nat. Med 15, 1170–1178 (2009). [PubMed: 19767732]
45. Coll RC et al. A small-molecule inhibitor of the NLRP3 inflammasome for the treatment of inflammatory diseases. Nat. Med 21, 248–255 (2015). [PubMed: 25686105]

Author Manuscript Author Manuscript Author Manuscript Author Manuscript

46. Brewer JM et al. Aluminium hydroxide adjuvant initiates strong antigen-specific Th2 responses in the absence of IL-4-or IL-13-mediated signaling. J. Immunol 163, 6448–6454 (1999). [PubMed: 10586035]
47. Garaude J, Kent A, van Rooijen N & Blander JM Simultaneous targeting of toll-and nod-like receptors induces effective tumor-specific immune responses. Sci. Transl. Med 4, 120ra116 (2012).
48. Guo Y, Lei K & Tang L Neoantigen vaccine delivery for personalized anticancer immunotherapy. Front. Immunol 9, 1499 (2018). [PubMed: 30013560]
49. Chu Y, Liu Q, Wei J & Liu B Personalized cancer neoantigen vaccines come of age. Theranostics 8, 4238 (2018). [PubMed: 30128050]
50. Li AW et al. A facile approach to enhance antigen response for personalized cancer vaccination. Nat. Mater 17, 528 (2018). [PubMed: 29507416]
51. Niikura K et al. Gold nanoparticles as a vaccine platform: influence of size and shape on immunological responses in vitro and in vivo. ACS nano 7, 3926–3938 (2013). [PubMed: 23631767]
52. Yang Y-Y, Chung T-S & Ng NP Morphology, drug distribution, and in vitro release profiles of biodegradable polymeric microspheres containing protein fabricated by double-emulsion solvent extraction/evaporation method. Biomaterials 22, 231–241 (2001). [PubMed: 11197498]
53. Ellens H, Bentz J & Szoka FC pH-induced destabilization of phosphatidylethanolamine-containing liposomes: role of bilayer contact. Biochemistry 23, 1532–1538 (1984). [PubMed: 6722105]

Author Manuscript Author Manuscript Author Manuscript Author Manuscript

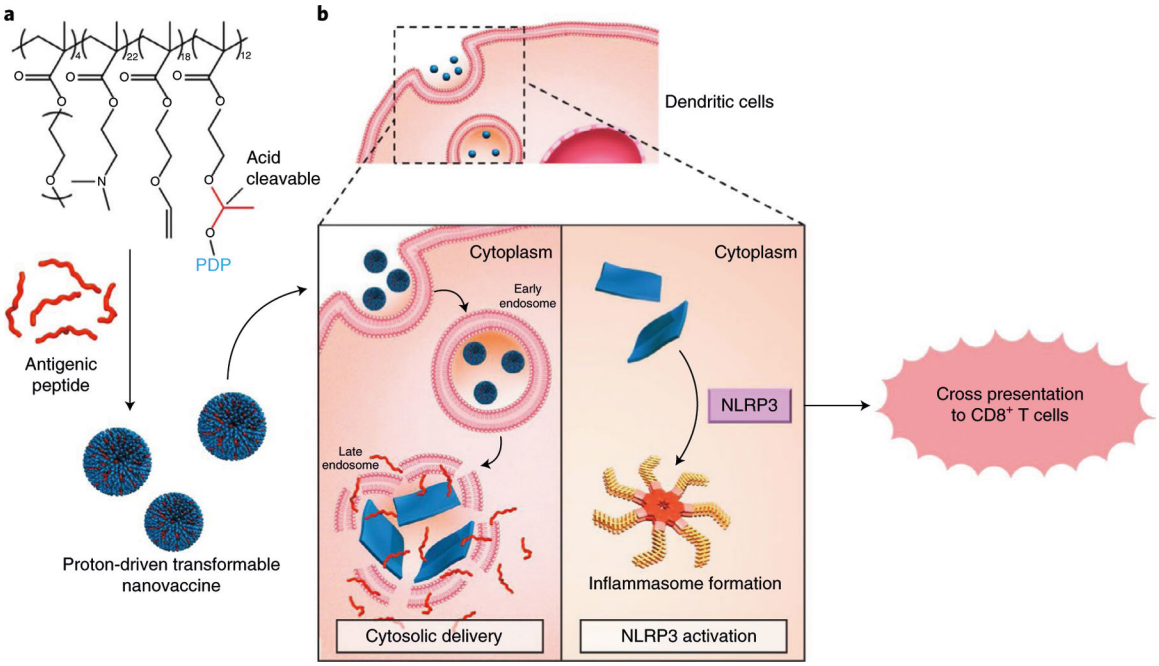

Fig. 1 |. Schematic illustration of a proton-driven NTV for cancer immunotherapy.

a, The NTV is composed of a polymer-peptide conjugate-based NT loaded with AP. The NTV has a spherical morphology with a diameter of about 100 nm at pH 7.4. **b**, After the NTV is internalized by DCs, the acidic endosomal environment (pH 5.6) will trigger fast cleavage of the PDP peptide, which will then re-assemble into nanosheets with sizes in the range 5–8 μm. The morphological change leads to disruption of the endosomal membrane and delivery of AP into the cytosol. Moreover, the cytoplasmic nanosheets activate the NLRP3 inflammasome pathway, which promotes DC maturation and antigen processing. These two features contribute to the enhanced cross-presentation of AP to $CD8^+$ T-cells and efficient antitumour immunity. PDP, pyrene-conjugated D-peptide; NLRP3, NOD-like receptor, pyrin-domain-containing 3.

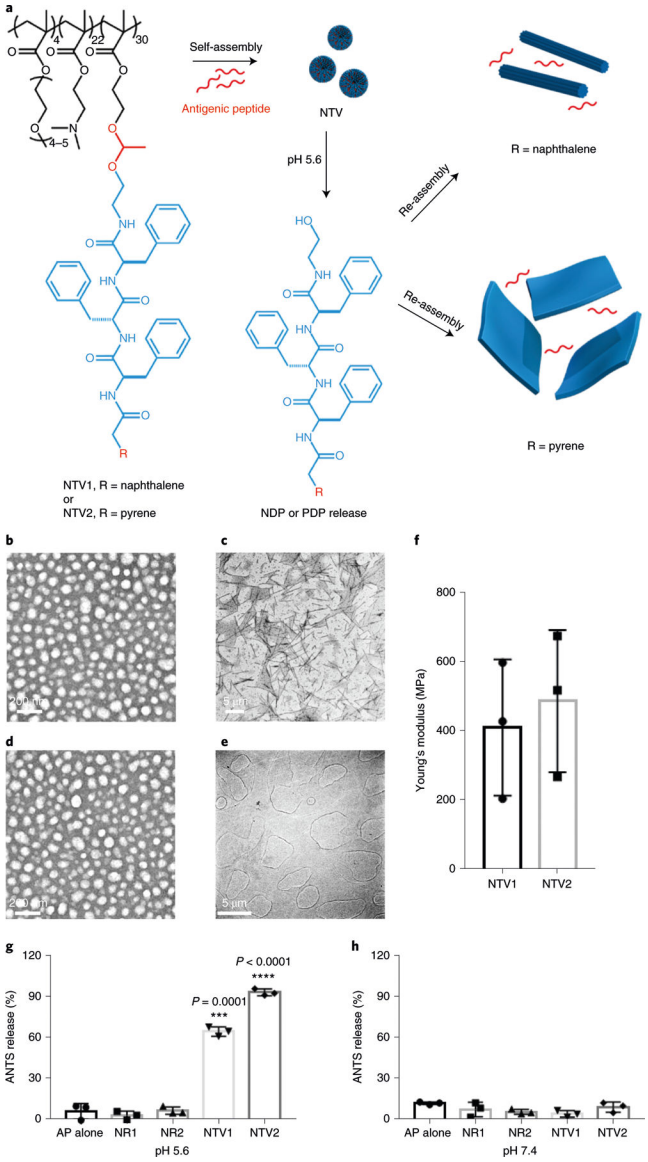

Fig. 2 |. Design and characterization of the NTV.

a, The NTV is composed of p(OEGMA$_4$-DMAEMA$_{22}$)-p(MA)$_{30}$ with conjugation of NDP or PDP with an acid-sensitive acetal bond. The polymer-peptide conjugates form nanospheres (about 100 nm) at physiological pH (pH 7.4). In a mimic endosomal acidic environment (pH 5.6), the acetal bond of NTV will be hydrolysed and the PDP or NDP peptide will be released from the polymer. The released peptides will re-assemble into nanofibres (NDP) or nanosheets (PDP) and induce the release of the cargo peptide from endosomes. **b**–**e**, TEM images of NTV1 (**b**, **c**) and NTV2 (**d**, **e**) at pH 7.4 (**b**, **d**) and pH 5.6 (**c**, **e**). Experiments in **b–e** were performed at least three times. TEM images in **b** and **d** were particles with negative staining using 2% uranyl acetate. Scale bars in **b** and **d** represent 200 nm; scale bars in **c** and **e** represent 5 μm. **f**, Young's modulus of the re-assembled nanofibres and nanosheets in a mimic endosomal environment (acetate buffer, pH 5.6); OVA$_{257–264}$ was used as a model AP in this experiment. Data were shown as means ± standard deviation

Author Manuscript Author Manuscript Author Manuscript Author Manuscript

Author Manuscript Author Manuscript Author Manuscript Author Manuscript

(s.d.) from three independent experiments. **g**,**h**, Evaluation of the endosomal disruption capacity of the different formulations in a dye-leakage experiment using mimic endosomes at pH 5.6 (**g**) and pH 7.4 (**h**); $OVA_{257–264}$ was used as a model AP in this experiment. The data are presented as means ± s.d. ($n = 3$) from three independent experiments, ****$P <$ 0.0001, ***$P = 0.0001$, by two-tailed Student's *t*-test (compared to the AP-alone group). We note that the 'sphere-to-nanofibre' nanotransformer is defined as NT1, the antigen peptide-loaded nanovaccine is defined as NTV1, and their pH-unresponsive counterparts are defined as NR1 and NRV1, respectively; the 'sphere-to-nanosheet' nanotransformer is defined as NT2, the antigen peptide-loaded nanovaccine is defined as NTV2, and their pH-unresponsive counterparts are defined as NR2 and NRV2, respectively. ANTS, the fluorophore 8-aminonaphthalene-1,2,3-trisulphonic acid.

Author Manuscript Author Manuscript Author Manuscript Author Manuscript

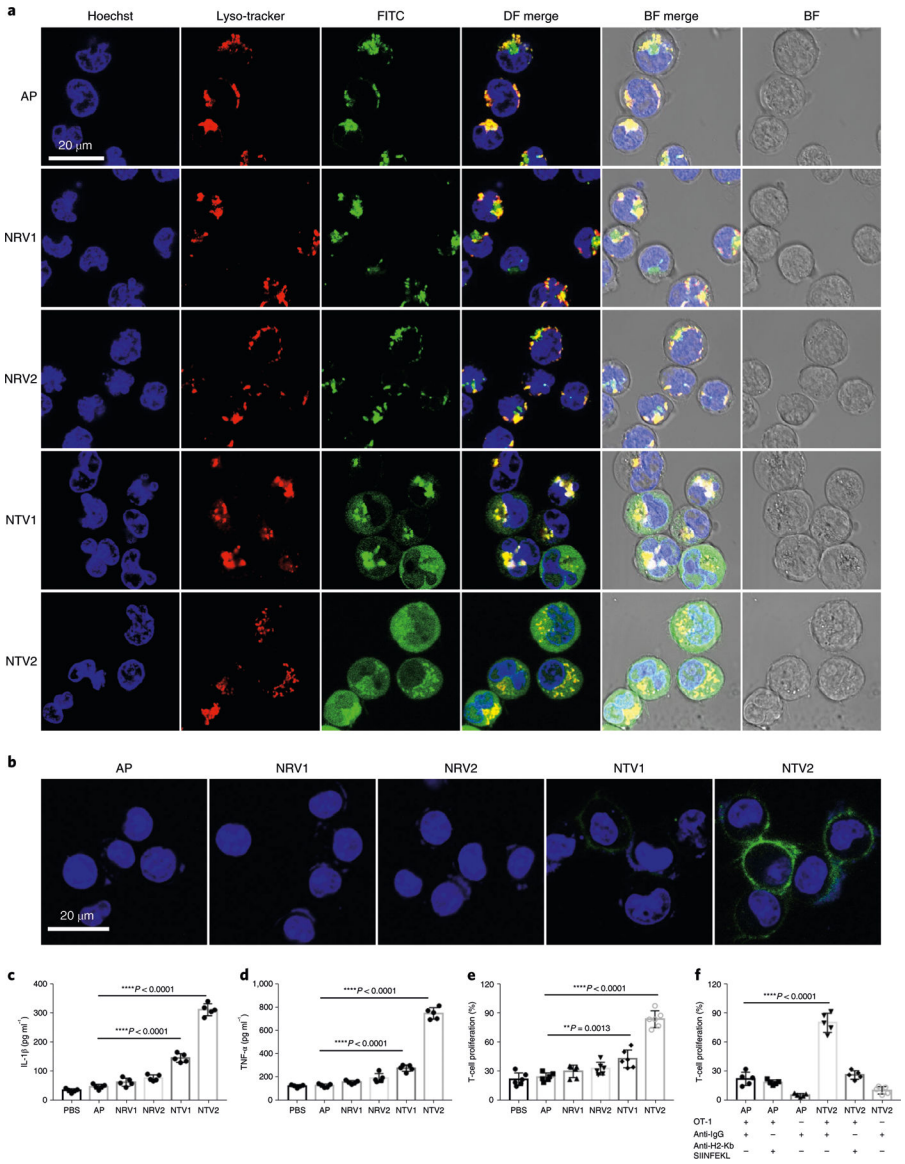

Fig. 3 |. NTV2 induces strong and sustained cross-presentation to CD8^{+} T-cells.

a, NTV-induced cytosolic delivery of AP in DC2.4 cells observed under confocal laser scanning microscopy (CLSM). DC2.4 cells were incubated with various formulations for 24 h and the distribution of OVA$_{241–270}$-FITC in the cells was observed under CLSM (scale bar: 20 μm). Experiments were performed at least three times. Blue, nucleus; red, late endosomes stained with Lyso-Tracker Deep Red; green, OVA$_{241–270}$-FITC. DF, dark field; BF, bright field. For the quantification[31] of fluorescence co-localization between AP-FITC and LysoTracker please see Supplementary Fig. 19a. **b**, Staining of the H-2K^{b}-OVA$_{257–264}$ complex to assess surface presentation of AP by DC2.4 cells after incubation with various formulations for 24 h (scale bar: 20 μm). Blue, nucleus; green, antibody against H-2K^{b}-OVA$_{257–264}$. Experiments were performed at least three times. **c**,**d**, Maturation of BMDCs after NTV treatment determined by measuring the secretion of IL-1β (**c**) or TNF-α (**d**). **e**, BMDCs were incubated with free AP, NRV1, NRV2, NTV1 or NTV2 for 4 h and washed

Author Manuscript Author Manuscript Author Manuscript Author Manuscript

five times with PBS. The BMDCs were then co-incubated with OT-I cells for another 72 h, and T-cell proliferation was assessed. **f**, Blocking the H-2K^{b}-OVA$_{257–264}$ on the surface of DCs reversed OT-I T-cell activation induced by NTV2-treated DCs. **c**–**f**, The data were shown as means ± s.d. (n = 5) from five independent experiments. ****P < 0.0001, **P = 0.0013, analysed by two-tailed unpaired Student's t-test.

Author Manuscript Author Manuscript Author Manuscript Author Manuscript

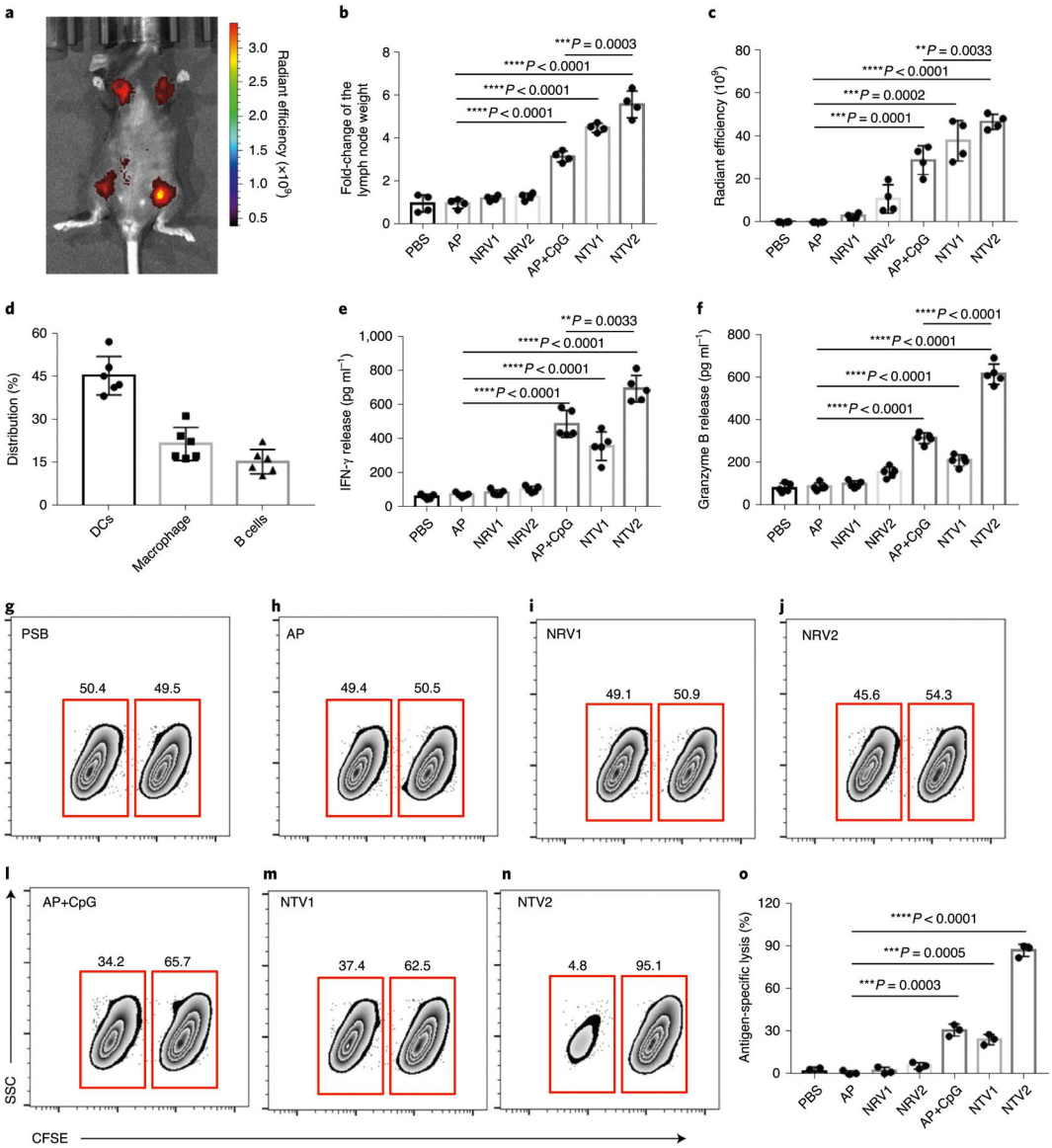

Fig. 4 |. NTV2 promotes aP delivery to lymph nodes and elicits cytotoxic lymphocyte responses. **a–c**, C57BL/6 mice were injected subcutaneously with various formulations at equivalent $OVA_{241–270}$-$Cy_{5.5}$ dose (5 μg per mouse). After 24 h, in vivo distribution of $OVA_{241–270}$-$Cy_{5.5}$ in nanovaccine-treated mice were detected (**a**), and the draining inguinal lymph nodes were isolated and the weight of lymph nodes were measured (**b**); data were shown as means ± s.d. ($n = 4$) from four independent experiments (two-tailed unpaired Student's *t*-test, ****$P < 0.0001$, ***$P = 0.0003$). The fluorescent signals in lymph nodes were quantified (**c**) with an in vivo imaging system. Experiments were conducted four times; data were shown as means ± s.d. ($n = 4$) from four independent experiments (two-tailed unpaired Student's *t*-test, ****$P < 0.0001$, ***$P = 0.002$ for AP versus NTV1 comparison, ***$P = 0.001$ for AP versus AP + CpG comparison, **$P = 0.0033$). CpG DNA, unmethylated cytosine-phosphorothioate-guanine oligodeoxynucleotides. **d**, NTV2 nanovaccine distribution in DCs, macrophage or B cells in lymph nodes. Experiments were conducted three times, data

Author Manuscript Author Manuscript Author Manuscript Author Manuscript

were shown as mean ± s.d. ($n = 6$) from six independent animals. **e**, **f**, Release of IFN-γ and Granzyme B from splenocytes of immunized C57BL/6 mice after ex vivo re-stimulation with SIINFEKL. Experiments were conducted three times, data were shown as means ± s.d. ($n = 5$) from five independent animals. Two-tailed unpaired Student's *t*-test, ****$P < 0.0001$, **$P = 0.033$. **g–o**, C57BL/6 mice were immunized with all the formulations three times (at 7-day intervals). One week after the last vaccination, $CFSE^{low}$ SIINFEKL-loaded and $CFSE^{high}$ non-loaded splenocytes were mixed (1:1) and intravenously injected into vaccinated mice. 24 h later, the splenocytes were analysed by flow. **g–n**, Representative flow plots in different treatment groups (gated on total splenocytes and then $CFSE^{+}$ cells). SSC, side scatter. **o**, Percentage of antigen-specific lysis for each treatment. Experiments were performed three times; data were shown as mean ± s.d. ($n = 3$) from three independent animals. Statistical significances were obtained by two-tailed unpaired Student's *t*-test: ****$P < 0.0001$, ***$P = 0.0005$ for AP versus NTV1 comparison, ** *$P = 0.0003$ for AP versus AP + CpG comparison.

Author Manuscript Author Manuscript Author Manuscript Author Manuscript

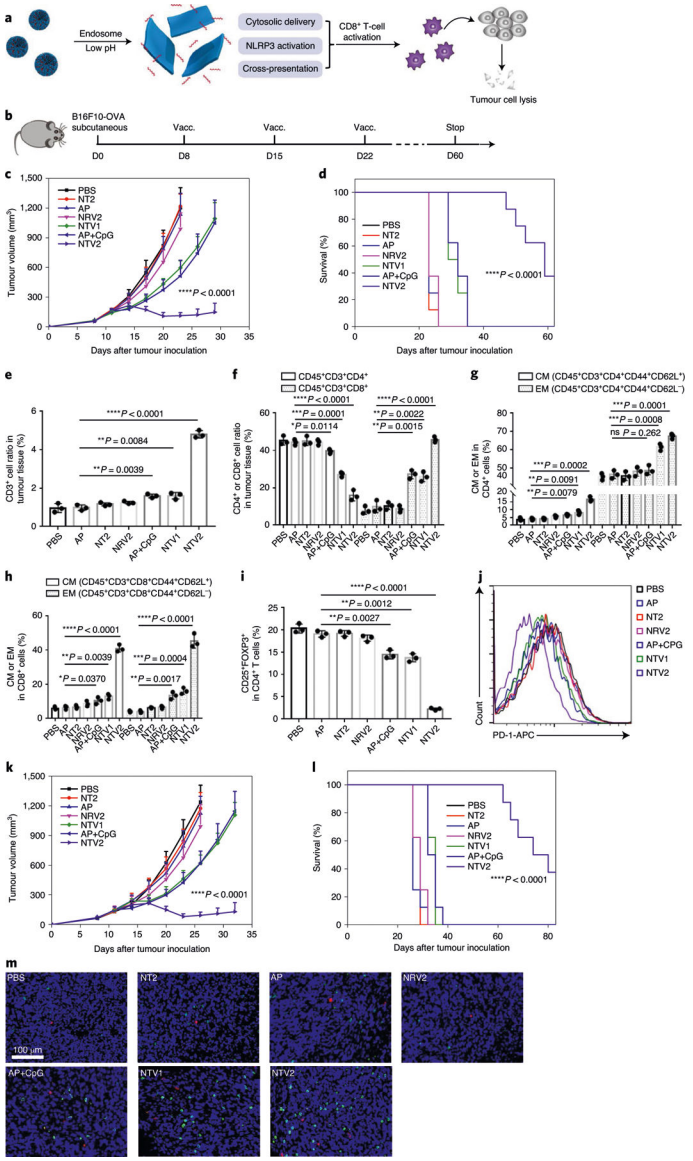

Fig. 5 |. NTV2 inhibits tumour growth and prolongs survival in tumour-bearing mice.

a, Illustration of the molecular transformation and mechanism of action of NTV2. **b**, The B16F10-OVA tumour model was established by subcutaneous injection of 1×10^6 B16F10-OVA cells into the right flank of female C57BL/6 mice. After the tumour volume reached 50 mm^3 (day 8), the mice were subcutaneously injected with AP alone, NTV2 (loaded with $OVA_{241–270}$) or other formulations at an equivalent AP dose of 5 μg per mouse. Injections were given 3 times at 7-day intervals. Saline was used as control. The tumour volumes (**c**) were measured every 3 days (data were shown as means ± s.d. ($n = 8$) from independent animals). **d**, Kaplan-Meier survival curves of mice in the different treatment groups in the B16F10-OVA model ($n = 8$ from independent animals). The PBS group (black line) was coincident with the NT2 group (red line). **e**,**f**, To investigate the mechanism under tumour growth inhibition, we performed another animal study to analyse the T-cell infiltration in the tumour tissue at day 23 using a flow cytometer. **e**, Average $CD45^+CD3^+$ T-cell ratio in the

Author Manuscript Author Manuscript Author Manuscript Author Manuscript

tumour tissue; data were shown as means ± s.d (n = 3) from three independent experiments (two-tailed unpaired Student's t-test, ****P < 0.0001, **P = 0.0084 for AP versus NTV1 comparison, **P = 0.0039 for AP versus AP + CpG comparison). **f**, $CD45^+CD3^+CD4^+$ or $CD45^+CD3^+CD8^+$ cell ratio in total T cells ($CD45^+CD3^+$); data were shown as means ± s.d (n = 3) from three independent experiments (two-tailed unpaired Student's t-test, ****P < 0.0001, ***P = 0.0001 **P = 0.0022 for AP versus NTV1 comparison, **P = 0.0015 for AP versus AP + CpG comparison, *P = 0.0114). **g**,**h**, $CD44^+CD62L^+$ CM cell or $CD44^+CD62L^-$ EM cell percentages in $CD45^+CD3^+CD4^+$ T cells or $CD45^+CD3^+CD8^+$ T cells, respectively. Data were shown as means ± s.d (n = 3) from three independent experiments. Two-tailed unpaired Student's t-test in **g**, ***P = 0.0002 for AP versus NTV2 comparison in CM, ***P = 0.0001 for AP versus NTV2 comparison in EM, ***P = 0.0008 for AP versus NTV1 comparison in EM, **P = 0.0091 for AP versus NTV1 comparison in CM, **P = 0.0079 for AP versus AP + CpG comparison in CM; ns, not significant P = 0.262. Two-tailed unpaired Student's t-test in **h**, ****P < 0.0001, ***P = 0.0004, **P = 0.0039 for AP versus NTV1 comparison, **P = 0.0017 for AP versus AP + CpG comparison, *P = 0.0370. **i**, $CD45^+CD3^+CD4^+CD25^+FOXP3^+$ Treg cell percentage in $CD45^+CD3^+CD4^+$ cells. Data were shown as means ± s.d (n = 3) from three independent experiments. Statistical significances were obtained by two-tailed unpaired Student's t-test: ****P < 0.0001, **P = 0.0012 for AP versus NTV1 comparison, **P = 0.0027 for AP versus AP + CpG comparison. **j**, Representative flow cytometric analysis of PD-1 expression on the surface of $CD45^+CD3^+$ T cells. Experiments were performed three times. **k**,**l**, Antitumour efficiency tested in human papillomavirus-E6/E7 tumour models. TC-1 tumour cells co-transfected with HPV-16 oncoproteins E6 and E7 and the c-Ha-ras oncogene were subcutaneously injected at day 0. When the tumour size reached about 50 mm^3 (at day 8), the mice were subcutaneously injected with free AP (E743–62, GQAEPDRAHYNIVTFCCKCD), NTV2 or other formulations at equivalent AP dose of 5 μg ml^{-1}. Injections were given three times at 7-day intervals. The tumour volumes (**k**) were measured every 3 days. **l**, Kaplan-Meier estimates of mice in the different treatment groups for the TC-1 tumour model. The PBS group (black line) was coincident with the NT2 group (red line). **m**, Representative immunofluorescence images of tumours showing $CD8^+$ (green) and $CD4^+$ (red) infiltration in the tumour tissues for all the treatment groups. Scale bar, 100 μm. Experiments were performed at least three times. In **c**, **d** and **k–l**, experiments were performed at least three times, data are shown as means ± s.d (n = 8) from independent repeats, compared by two-tailed unpaired Student's t-test: ****P < 0.0001. The statistical significance of animal survival in **d** and **l** was analysed by the log-rank test: ****P < 0.0001.

Author Manuscript Author Manuscript Author Manuscript Author Manuscript

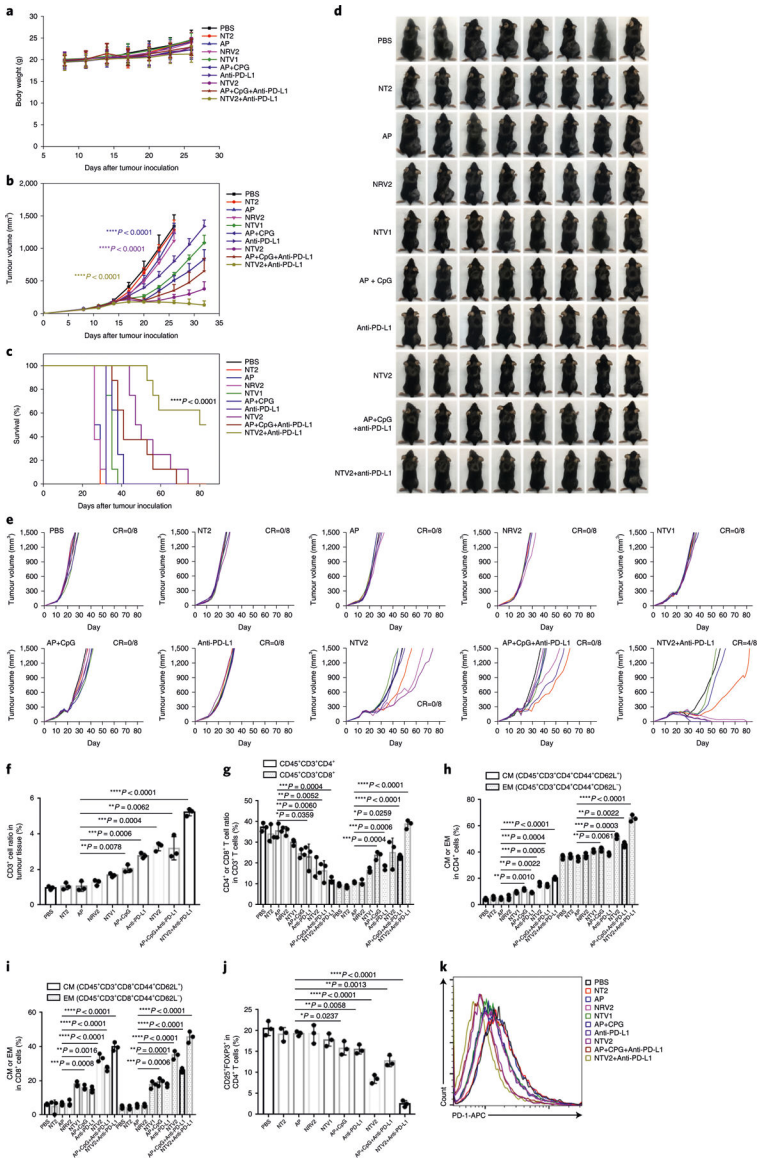

Fig. 6 |. Neoantigen peptide-loaded NTV2 in combination with anti-PD-L1 for efficient cancer immunotherapy in the B16F10 model.

A B16F10 tumour was constructed at day 0 by subcutaneous injection of 1×10^6 B16F10 cells and mice were randomly divided into ten groups. Mice were given subcutaneous injection of AP, NTV2 and various vaccine formulations at an equivalent AP dose of 5 μg ml $^{-1}$ were used (a mixture of B16-M27, B16-M30, B16-M47 and B16-M48 as AP; for detailed sequence information please see Supplementary Information) or intraperitoneal injection of anti-PD-L1 (100 μg per mouse) at days 8, 15 and 22. **a**, Average body weight of mice in different treatment groups, measured every 3 days. Data were shown as means ± s.d. ($n = 8$) from eight independent animals. The tumour volumes (**b**) were measured every 3 days. Data were shown as mean ± s.d. ($n = 8$) from eight independent animals. Statistical significances were obtained by two-tailed unpaired Student's *t*-test: ****$P < 0.0001$. **c**, Kaplan-Meier estimates of mice in the different treatment groups in the B16F10 tumour model (statistical significance was analysed by the log-rank test: ****$P < 0.0001$, from eight independent

Author Manuscript Author Manuscript Author Manuscript Author Manuscript

animals). The PBS group (black line) was coincident with the NRV2 group (pink line, before day 29) and NT2 (red line, after day 32). **d**, Photographs of mice in the different treatment groups at day 26. **e**, Individual B16F10 tumour size curves in the different treatment groups are shown. To investigate the mechanism of tumour growth inhibition, we performed another animal study to analyse T-cell infiltration in the tumour tissue at day 26 using a flow cytometer. CR, complete tumour regression. **f**, Average $CD45^+CD3^+$ T-cell ratio in the tumour tissue; data were shown as means ± s.d ($n = 3$) from three independent experiments. Statistical significances were obtained by two-tailed unpaired Student's *t*-test: ****$P < 0.0001$, ***$P = 0.0004$ for AP versus NTV2 comparison, ***$P = 0.0006$ for AP versus anti-PD-L1 comparison, **$P = 0.0062$ for AP versus AP + CpG + anti-PD-L1 comparison, **$P = 0.0078$ for AP versus AP + CpG comparison. **g**, $CD45^+CD3^+CD4^+$ or $CD45^+CD3^+CD8^+$ cell ratio in total T cells ($CD45^+CD3^+$), data were shown as means ± s.d ($n = 3$) from three independent experiments. Statistical significances were obtained by two-tailed unpaired Student's *t*-test: ****$P < 0.0001$, ***$P = 0.0004$ for AP versus NTV2 + anti-PD-L1 comparison in $CD45^+CD3^+CD4^+$ cells, ***$P = 0.0006$ for AP versus anti-PD-L1 comparison in $CD45^+CD3^+CD8^+$ cells, ***$P = 0.0004$ for AP versus AP^+CpG comparison in $CD45^+CD3^+CD8^+$ cells, **$P = 0.0052$ for AP versus AP + CpG + anti-PD-L1 comparison in $CD45^+CD3^+CD4^+$ cells, **$P = 0.0060$ for AP versus NTV2 comparison in $CD45^+CD3^+CD4^+$ cells, *$P = 0.0359$ for AP versus $anti^-PD$-L1 comparison in $CD45^+CD3^+CD4^+$ cells, *$P = 0.0259$ for AP versus NTV2 comparison in $CD45^+CD3^+CD8^+$ cells. **h-i**, $CD44^+CD62L^+$ CM T cell or $CD44^+CD62L^-$ EM cell percentages in $CD45^+CD3^+CD4^+$ T cells or $CD45^+CD3^+CD8^+$ T cells, respectively. Data were shown as means ± s.d ($n = 3$) from three independent experiments. Statistical significances in **h** were obtained by two-tailed unpaired Student's *t*-test: ****$P < 0.0001$, ***$P = 0.0004$ for AP versus AP + CpG + anti-PD-L1 comparison in CM, ***$P = 0.0005$ for AP versus NTV2 comparison in CM, ***$P = 0.0003$ for AP versus NTV2 comparison in EM, **$P = 0.0010$ for AP versus AP + CpG comparison in CM, **$P = 0.0022$ for AP versus anti-PD-L1 comparison in CM, **$P = 0.0022$ for AP versus AP + CpG + anti-PD-L1 comparison in EM, **$P = 0.0061$ for AP versus AP + CpG comparison in EM. Statistical significances in **i** were obtained by two-tailed unpaired Student's *t*-test: ****$P < 0.0001$, ***$P = 0.0008$ for AP versus AP + CpG comparison in CM, ***$P = 0.0001$ for AP versus anti-PD-L1 comparison in EM, ***$P = 0.0006$ for AP versus AP + CpG comparison in EM, **$P = 0.0016$ for AP versus anti-PD-L1 comparison in CM. **j**, $CD45^+CD3^+CD4^+CD25^+FOXP3^+$ Treg-cell percentage in $CD45^+CD3^+CD4^+$ cells. Data were shown as means ± s.d ($n = 3$) from three independent experiments. Statistical significances were obtained by two-tailed unpaired Student's *t*-test: ****$P < 0.0001$, **$P = 0.0013$ for AP versus AP + CpG + anti-PD-L1 comparison, **$P = 0.0058$ for AP versus anti-PD-L1 comparison, *$P = 0.0237$. **k**, Representative flow cytometric analysis of PD-1 expression on the surface of $CD45^+CD3^+$ T cells.